Article

Detection of lithium in the exosphere of Mercury

Daniel Schmid [1,5] ✉, Helmut Lammer [1,5], Alexey A. Berezhnoy [2], Fabian Weichbold[1], Manuel Scherf [1], Ali Varsani [1], Martin Volwerk[1], Cyril Simon-Wedlund [1], Wolfgang Baumjohann[1], Rumi Nakamura[1], Go Murakami[3] & Ferdinand Plaschke [4]

Mercury's exosphere contains various neutral species, including hydrogen, helium, sodium, potassium, calcium, magnesium, aluminum, iron, and manganese. Although lithium has been predicted to exist, it had not been detected until now. Here, we demonstrate the presence of lithium in Mercury's exosphere, using data from the Mercury Surface, Space ENvironment, GEochemistry, and Ranging spacecraft. The sporadic detection of lithium suggests its meteoritic origin, likely released through evaporation caused by sporadic meteoroid impacts. Our findings provide strong evidence supporting the hypothesis that (micro-)meteoroids and larger meteoroids, which have continuously and sporadically impacted Mercury's surface over billions of years, are a significant source of volatile elements and contributed substantially to Mercury's unexpectedly volatile-rich surface. This detection emphasizes the significant role of meteoroids in shaping Mercury's exosphere and provides insights into the planet's evolution and the history of volatile elements in the Solar System.

Mercury, the innermost planet of our solar system, is encompassed by a collisionless exosphere. This exosphere consists of various species originating from the solar wind, (micro-)meteoroid impacts, and interactions with the planetary surface. Based on ground-based and spacecraft observations of the Mariner 10 spacecraft in 1974/75[1] and, four decades later, by the MErcury Surface, Space ENvironment, GEophysics and Ranging[MESSENGER; 2] spacecraft, the exosphere is known to contain H, He, Na, K, Ca, Mg, Al, Fe, and Mn[3]. Early estimates from the Mariner 10 occultation experiment already suggested that Mercury's total exospheric surface pressure is expected to be higher than that calculated from the known exospheric species[4], indicating that Mercury likely contains several unknown exospheric species as well[5]. After the discoveries of the lithophile elements sodium (Na) and potassium (K) in Mercury's exosphere[6,7], it has been speculated that a

low abundance of lithium (Li) may be present in the exosphere, where some fraction originates from infalling micrometeoritic material and the rest results from lithospheric surface materials[8]. In Earth's atmosphere, the major source of Na, K, and Li is meteoritic evaporation[9].

While on Earth, small meteoroids that contribute these elements to the atmosphere typically do not reach the surface, the lack of a dense atmosphere on Mercury allows these meteoroids to consistently impact the surface. Consequently, the surface of Mercury is continuously bombarded by (micro-)meteoroids and, less frequently, by centimeter- to meter-sized meteoroids[10]. In 2013, MESSENGER observed a rare event where a significant enhancement at high altitudes of the exosphere occurred due to the impact vaporization of sodium caused by the impact of meter-sized meteoroid[11]. This impacting material adds meteoritic elements to the upper regolith,

[1]Space Research Institute (IWF), Austrian Academy of Sciences (OeAW), Schmiedlstrasse 6, Graz 8010, Austria. [2]Sternberg Astronomical Institute, Moscow State University, Universitetskij pr. 13, Moscow 119991, Russian Federation. [3]Department of Solar System Science, Institute of Space and Astronautical Science (ISAS), 3-1-1 Yoshinodai, Chuo, Sagamihara, Tokyo 252-5210 Kanagawa, Japan. [4]Institut für Geophysik und extraterrestrische Physik (IGEP), Technische Universität Braunschweig (TUBS), Mendelssohnstraße 3, Braunschweig 38106, Germany. [5]These authors contributed equally: Daniel Schmid, Helmut Lammer. ✉e-mail: daniel.schmid@oeaw.ac.at
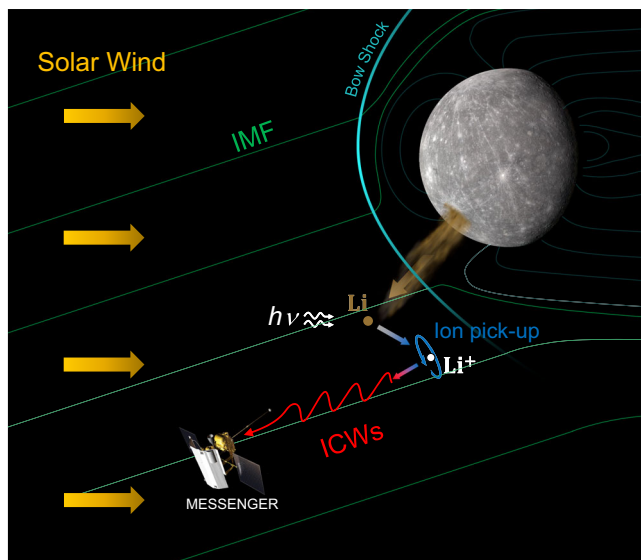
Fig. 1 | Illustration of the generation mechanism of pick-up ion cyclotron waves in Mercury's space environment. Lithium (Li) released through (micro-)meteoroid evaporation at the surface can ascend beyond Mercury's planetary magnetic field (depicted by blue lines) and the bow shock (light blue arc), reaching the solar wind region where it becomes photoionized by the Sun's extreme ultraviolet radiation, characterized by the light frequency, v times Planck's constant, h. The freshly ionized Li^+ starts to gyrate in the presence of the interplanetary magnetic field (IMF) and gets picked up by the background solar wind. The solar wind plasma becomes unstable, which excites the ion cyclotron waves (ICWs) that are subsequently detected by the MESSENGER spacecraft. The display elements are not to scale. Credit: The MESSENGER spacecraft and Mercury images are provided by NASA/Johns Hopkins APL/Carnegie Institution of Washington.

causing it to mix and vitrify in a manner akin to processes observed on the Moon. Apollo drill cores of the Lunar surface material show for example non-monotonic variations in the composition of the upper meter of the regolith[12,13]. At the meteor impact site, the regolith's upper surface layers underwent a transformation that creates a melt phase, solid ejecta, and a vapor phase where surface material and meteoritic material are released into the lunar exosphere. Also at Mercury, meteoroids are one of the sources for the exosphere formation[14]. While a portion of the meteoritic elements escapes as neutrals or ions, a fraction is retained on the surface[5].

So far, however, the presence of Li has not been confirmed at Mercury. Neither in-situ particle measurements onboard Mariner10 and MESSENGER, nor remote observations with telescopes could prove the presence of Li. Because of the non-detection with the 1.5-m telescope at the Catalina Observatory, Arizona, the upper limit of the Li surface column density was expected to be less than 8.4×10^7 cm^{-2}[15], which is in the same order of magnitude estimated from the non-detection with the European Southern Observatory-New Technology Telescope observations at La Silla, Chile[16].

Previous studies on comets[17], Mars[18], and Venus[19], alongside the recent discoveries on Mercury[20], have shown the existence of exospheric elements at all of these bodies based on the detection of so-called pick-up ion cyclotron waves (ICWs) in the in-situ magnetic field measurements. Pick-up ion cyclotron waves (ICWs) are transverse electromagnetic waves that propagate nearly parallel to the ambient magnetic field. Their polarization, either left- or right-hand elliptical, is determined by the pick-up geometry of freshly ionized neutrals. Left-handed waves are primarily generated when the magnetic field is oriented perpendicular to the plasma flow, whereas right-handed waves dominate when the magnetic field aligns parallel to the flow. At Mercury's orbit within the solar wind, right-handed polarized ICWs are preferentially excited due to the relatively small angle (approximately

30°) between the interplanetary magnetic field and the solar wind's flow direction[20,21]. These waves travel sunward with a phase velocity roughly equal to the Alfvén speed,

$$V_A = B_0 / \sqrt{\mu_0 \rho}, \qquad (1)$$

with B_0 the background magnetic field strength, μ_0 the permeability of free space and ρ the mass density of the charged particles in the plasma. The propagation speed of these waves is lower than the solar wind velocity, causing them to be advected in the anti-sunward direction across the spacecraft. In the spacecraft's frame of reference, the waves exhibit left-hand polarization and are consistently detected at the local ion gyrofrequency. This is due to the negligible velocity of newly introduced exospheric ions relative to the spacecraft. As a result, any potential misidentification with plasma waves generated at the bow shock by back-streaming solar wind protons is eliminated, since the latter are observed at significantly different frequencies due to their substantial velocity relative to the spacecraft[19,22].

In this work, we report the observation of pick-up ICWs generated by the solar wind pick-up of freshly ionized Li atoms. We analyze MESSENGER's magnetic field data in the solar wind to identify ICWs and use the observed wave power to infer the local density of Li required to produce these waves. Applying a Chamberlain exospheric model[23], we provide insights into the origin of these Li particles, which are released from Mercury's surface through evaporation of sporadic meteoroid impacts. Upon photoionization, these neutral Li atoms gyrate around the interplanetary magnetic field and are subsequently picked up by the solar wind. The velocity difference between the newly formed Li ions and the solar wind plasma creates an instability, leading to the excitation of the pick-up ICWs[24]. A schematic illustration of this pick-up ICW generation mechanism is presented in Fig. 1.

Results
Detection of lithium pick-up cyclotron waves
To identify ion cyclotron waves (ICW) that specifically originate from the pick-up of newly-born Li^+ ions, we adopt the selection criteria that have successfully been used for the identification of ICWs generated from freshly ionized hydrogen around Mercury[20].

Because the abundance of ^6Li is negligible compared to ^7Li[25] we adapt the procedure to the heavier ion. To ensure that the observed waves are freshly generated from local ion pick-up[26], we preselect intervals where the MESSENGER spacecraft was located in the solar wind on the dayside with respect to the terminator.

In Fig. 2, an example of an identified Li^+ ion cyclotron wave is shown. Figure 2a shows the magnetic field observation in mean-field aligned (MFA) coordinates, where $B_\parallel$ denotes the parallel component and $B_{\perp,1}$ and $B_{\perp,2}$ the perpendicular components with respect to the background magnetic field. The two perpendicular components (red and blue) exhibit a strong degree of coherence, and their fluctuations are stronger than the parallel magnetic field variations (orange). This is also evident from the power spectral density in Fig. 2b, where the perpendicular power density, determined by the two perpendicular components (black) dominates over the parallel power density (orange), indicating that the observed wave is rather transverse than compressional around the Li^+ cyclotron frequency f_{c,Li^+} of approximately 0.05 Hz (marked as a dashed black line). The gray shaded area depicts the frequency range ΔF, used to evaluate the characteristics of the ICWs. Figure 2c shows the hodogram of the time interval. The observed wave is planar in the transverse direction to the background magnetic field and nearly circular in the $(B_{\perp,1}, B_{\perp,2})$-plane. The orange star and cyan diamond mark the start and end times of the time interval, clearly showing the left-handed rotation of the wave about the background magnetic field.
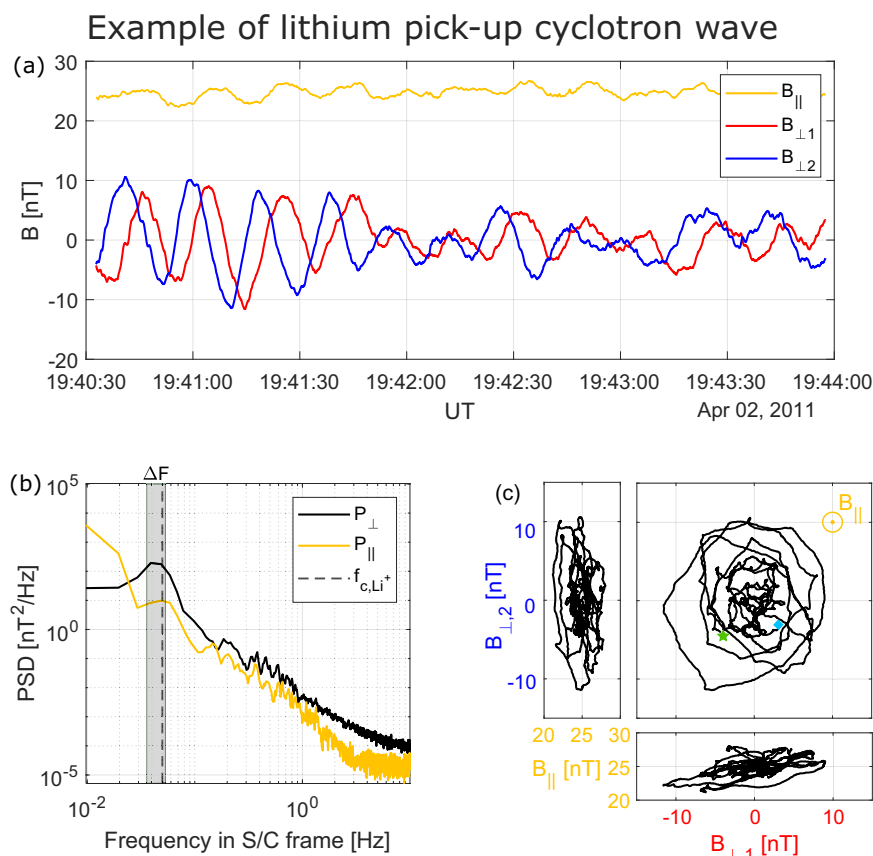
Example of lithium pick-up cyclotron wave

Fig. 2 | Example of an identified Li ion cyclotron wave (ICW). a Magnetic field observations in mean-field-aligned (MFA) coordinates. $B_\parallel$ denotes the parallel magnetic field component (orange), while $B_{\perp,1}$ (blue) and $B_{\perp,2}$ (red) represent the perpendicular magnetic field components. **b** Power spectrum of the parallel (orange) and the two perpendicular (black) magnetic field components. The dashed black line denotes the local lithium cyclotron frequency f_{c,Li^+} and the gray shaded area depicts the frequency range ΔF, used to evaluate the characteristics of the ICWs. **c** Hodogram of the magnetic field components in MFA coordinates. The green star and cyan diamond in the $(B_{\perp,1}, B_{\perp,2})$-plane mark the start and end times of the time interval. Source data are provided as a Source Data file.

Estimation of the local lithium density

From the observed wave power of the ICWs we can derive the required neutral Li densities with a method similar to the one successfully used for atomic hydrogen at Mercury[27]. The total free energy, E_{free}, which is required to excite the cyclotron waves, is approximately given by[17]:

$$E_{free} = \frac{1}{4} m_{Li} n_{Li^+} V_A V_{inj} \left[(1 + \cos(\alpha))^2 + (1 - \cos(\alpha))^2 \right]. \quad (2)$$

Here, $m_{Li} = 6.941\,u = 1.16 \times 10^{-23}\,g$ and n_{Li^+} are the mass and density of the pick-up Li$^+$ ions. V_A is the local Alfvén velocity, V_{inj} is the injection velocity of the Li$^+$ ions into the solar wind and $\alpha = \angle(\mathbf{V}_{inj}, \mathbf{B}_0)$ is the angle between the injection velocity and the background magnetic field vector. Inverting Eq. (2) for n_{Li^+} yields the pick-up ion density, under the assumption that the entire free energy of the newly-born pick-up ions is transferred to the wave growth. Computer simulations, however, show that only a fraction of the energy is transferred to the wave so that

$$E_{free} = \Phi \cdot E_{ICW}, \quad (3)$$

where Φ describes the efficiency of the energy transfer ($\Phi \leq 1$) and

$$E_{ICW} = \int_{\Delta F} P_\perp \, df, \quad (4)$$

is the observed wave energy determined by the power spectral density of the perpendicular magnetic field components around the local Li$^+$

gyrofrequency (see e.g., Fig. 2). For heavy ions, an efficiency factor of Φ of approximately 0.3 is realistic[28]. Since the pick-up ion density is balanced by the ion production rate, which can be estimated by multiplying the neutral Li density n_{Li} by the photoionization rate, $k_{h\nu}$, it is possible to derive the neutral Li density from the estimated ion densities n_{Li^+} from Eq. (2) with:

$$n_{Li} = \frac{n_{Li^+} \cdot \Omega_{Li^+}}{100 \cdot k_{h\nu}}. \quad (5)$$

We use the characteristic time ($\Omega_{c,Li^+} \cdot t$) of 100 gyroperiods until the ICWs are fully developed and a quasi-steady state is reached. The (conservative) assumption of 100 gyroperiods is motivated by computer simulations that have shown that the full energy transfer from the ions to the waves takes approximately 60–100 ion gyrations[29]. Since the photoionization rate significantly varies with the solar activity and the radial distance of Mercury to the Sun, we also adapt $k_{h\nu}$ for each ICW event accordingly.

By surveying four years of MESSENGER data, we identified 12 ICW events near the local Li$^+$ gyrofrequency. The results of our detection and analysis are shown in Table 1 and Fig. 3.

Figure 3 depicts the radial observation distance, measured from both, the planetary center in Mercury radii ($R_M = 2440$ km) (top axis), and the planetary surface (bottom axis), pertaining to the 12 independent events alongside their estimated neutral Li number densities. The black error bars are the 95% quantiles determined from a Monte Carlo error analysis of Eqs. (2) and (5).

Table 1 | Summary of the observation times, locations, and estimated Li densities for the 12 identified ICW events

Time [UTC]	TAA	LT	Lon	Lat	Alt [km]	n_{Li} [cm^{-3}]	n_O [cm^{-3}]	N [cm^{-2}]
2011-04-02 19:41	94°	11:10	−12°W	− 69°S	14,525	1.51×10^{-3}	5.1×10^{-2}	0.61×10^{7}
2011-04-03 07:41	96°	10:59	−15°W	− 70°S	14,453	2.24×10^{-3}	10.7×10^{-2}	1.27×10^{7}
2011-04-03 08:56	96°	11:25	−8°W	− 62°S	15,175	0.91×10^{-3}	10.2×10^{-2}	1.21×10^{7}
2011-04-03 11:45	97°	11:51	−2°W	− 42°S	12,842	1.40×10^{-3}	6.4×10^{-2}	0.76×10^{7}
2011-12-26 18:15	110°	09:34	−36°W	− 75°S	14,676	1.55×10^{-3}	10.0×10^{-2}	1.19×10^{7}
2012-03-05 16:26	19°	16:57	74°E	− 22°S	5873	6.76×10^{-3}	5.0×10^{-2}	0.60×10^{7}
2012-05-27 19:04	348°	17:03	75°E	− 77°S	10,250	4.87×10^{-3}	15.1×10^{-2}	1.80×10^{7}
2012-11-30 15:08	56°	14:30	38°E	− 13°S	3312	13.22×10^{-3}	5.9×10^{-2}	0.70×10^{7}
2012-12-01 20:52	61°	12:57	14°E	− 71°S	9599	3.51×10^{-3}	11.0×10^{-2}	1.31×10^{7}
2013-05-01 01:59	274°	12:20	5°E	− 46°S	6391	3.87×10^{-3}	7.6×10^{-2}	0.91×10^{7}
2014-01-13 13:01	248°	14:29	37°E	− 66°S	9958	1.67×10^{-3}	7.9×10^{-2}	0.94×10^{7}
2014-07-24 07:16	322°	08:19	−55°W	7°N	2670	8.33×10^{-3}	4.9×10^{-2}	0.58×10^{7}

TAA indicates Mercury's True Anomaly Angle during the ICW observation. LT, Lon, Lat, and Alt denote the local time, longitude, latitude, and altitude of MESSENGER during the event. The Li surface density (n_O) and vertical column density (N) are derived from the neutral Li number density (n_{Li}), as estimated in Eq. (5), using a Chamberlain model for a near-surface temperature of $T_O = 3750$ K.
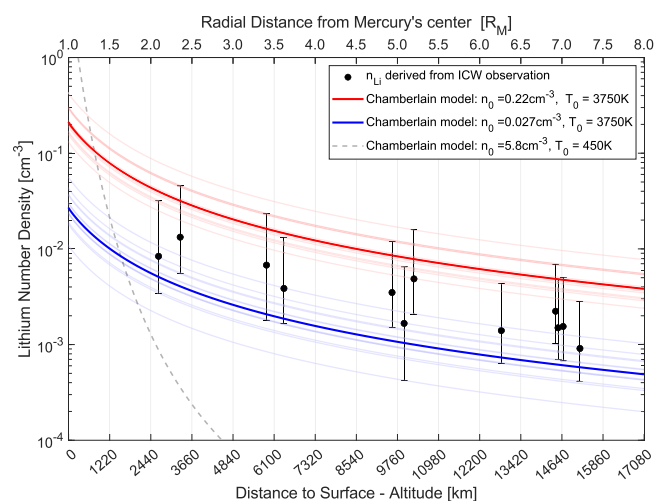

Fig. 3 | Radial observation location of the 12 events alongside their Li density. Black dots are the neutral Li number density derived from the ICW observation, using Eqs. (2) and (5). The error bars are the 95% quantiles determined from a Monte Carlo error analysis on the determined Li densities. The transparent red (blue) lines illustrate Chamberlain models fitted to the upper (lower) error bar value for each event individually, with the opaque lines indicating the median of these fits. The dashed gray line depicts the Chamberlain profile for an average surface temperature of 450 K and the upper limit of the surface density based on the non-detection by remote instruments. Source data are provided as a Source Data file.

Potential origin of lithium at Mercury

Basically, Mercury's exosphere is predominantly sustained through four main mechanisms: thermal desorption, photon-stimulated desorption, ion sputtering, and impact vaporization[30]. Thermal desorption and photon-stimulated desorption release atoms due to heating and photon bombardment of the surface, respectively, which produce atoms with insufficient energies to reach high altitudes. Ion sputtering and impact vaporization involve ion impacts from the solar wind particles and high-energy impacts of (micro-) meteoroids, respectively, and can produce high energetic particles that can reach high altitudes.

To further analyze which mechanism was responsible for the detection of Li, we apply a Chamberlain exospheric model[23], which is commonly used to model Mercury's exospheric populations[5,31,32]. In this model, the only controlling factors considered are the gravitational attraction and the near-surface density and temperature of the exospheric particle population[32].

The dashed gray line in Fig. 3 depicts the Chamberlain profile for an average dayside surface temperature of $T_O = 450$ K and the upper limit of the expected surface density based on the non-detection by remote instruments which is $n_O = 5.8$ cm^{-3}[15]. Given that the surface density must be less than this threshold (as otherwise, remote instruments would have detected Li), thermal desorption of Li from the surface cannot account for the extended observation location of the events. Just like thermal desorption, photon-stimulated desorption generates atoms with energy levels too low to reach high altitudes. Therefore, it is not considered a significant contributor.

Ion sputtering leads to high escape rates, driven by solar wind and/or energetic magnetospheric ions[30]. Magnetic reconnection, which occurs under antiparallel orientations of the interplanetary magnetic field (IMF) and planetary magnetic field, enhances sputtering by directing solar wind particles and/or energizing magnetospheric ions. These particles travel along reconnected field lines to the planetary surface, potentially sputtering upward-moving surface particles[33]. Prolonged antiparallel IMF alignment reduces the dayside magnetic field's shielding, allowing increased solar wind ion precipitation and further sputtering[34]. These effects are particularly significant during strong solar wind events, where precipitation rates significantly increase[35]. A brief examination of interplanetary coronal mass ejection (ICME) MESSENGER observations at Mercury[36], whether sputtering due to ICME collisions with the planet could have been responsible during the time of the observed Li enhancements, shows that only one event occurred during an ICME (March 5, 2012) and two events (May 27, 2012; May 1, 2013) occurred several hours before and after an ICME. Typically, the ballistic time scales before the sputtered particles are lost to the surface or carried away by the solar wind extend to a couple of hours following a significant impulsive ion precipitation event[35,37]. Given the significant presence of ICMEs during the four-year observation period of the MESSENGER mission, it is reasonable to anticipate that Li events would be consistently observed across a wide range of the spacecraft's orbit. However, the observed Li events are only detected within a few minutes and very rarely, suggesting that they are unlikely to be associated with magnetic reconnection, since the orientation of the interplanetary magnetic field is highly variable[21], and thus magnetic reconnection occurs frequently. Thus, observed Li events are unlikely to be connected to ICMEs and/or antiparallel IMF conditions directly and sputtering is considered unlikely to be the source of the detected Li.

Consequently, impact vaporization, caused by high-energy impacts, appears to be the most likely explanation for the observed

events. In fact, the sporadic occurrence of the events and their short observation periods correspond well to the ballistic time scales of tens of minutes after meteoroid impact vaporization[38].

Following studies of the chemistry of impact-produced vapor clouds, Li is delivered to the exosphere mainly in the form of Li atoms during meteoroid impacts[39]. In this case, the kinetic temperature of Li atoms is close to 2500–5000 K, which has also been inferred from hypervelocity impact experiments[40]. To estimate the Li surface density required to produce the derived Li densities in the exosphere, we applied a Chamberlain model, assuming an average meteoritic impact-related cloud temperature of 3750 K for each event individually. Specifically, we performed a least-squares fit of the Chamberlain model to the upper and lower error margins of the inferred Li densities for each event. The resulting profiles are illustrated in Fig. 3 with transparent red (blue) lines for the upper (lower) error margin. The median of the Chamberlain profiles (red and blue lines in Fig. 3) subsequently determines the expected average surface density range, which is $n_0 = 0.03$–0.2 cm^{-3}. Notably, all 12 events fall within this range, even though they are independent, indicating that the observed Li number densities can be accurately reproduced under meteoroid impact-related cloud temperatures.

Table 1 provides a summary of the observation time (UTC) and observation locations of the 12 ICW events. The events are observed to be evenly distributed throughout the Mercury year, as evidenced by the uniformly distributed true anomaly angles (TAA) of Mercury around the Sun. Furthermore, the geographic observation locations of the events do not exhibit a clear trend, as the local time (LT) and corresponding longitude (Lon) of the S/C during the event observation are uniformly distributed across the dayside of Mercury. The fact that the majority of events are detected in the southern hemisphere, indicated by the negative latitude (Lat), is attributable to the S/C orbital path, as MESSENGER exhibits a highly elliptical orbit, with its periherm located at the geographic north (shorter dwelling time in this region of its orbit) and its apoherm situated far into the geographic south (longer dwelling time in this region of its orbit). To obtain the Li surface density (n_0) during the detected events, a least squares fit of a Chamberlain profile was applied to the inferred Li densities (n_{Li}) for the case of a near-surface temperature of $T_0 = 3750$ K. The black dots represent individual observations recorded at various times during the MESSENGER mission and, as such, do not constitute a measured radial profile. However, within the context of this analysis, it is reasonable to treat them as a radial profile. Utilizing the derived surface number densities and giving that the average vapor cloud temperature, T_{vc}, near the surface is about 3750 K, the vertical Li column density (N) can be determined through

$$N = n_0 \cdot H, \quad (6)$$

where H represents the characteristic scale height

$$H = (k_B \cdot T_{vc})/(m_{Li} \cdot g_{pl}), \quad (7)$$

with k_B denoting the Boltzmann constant and $g_{pl} = 3.78$ m/s^2 the gravitational acceleration on Mercury.

Discussion

Considering that the average temperature of the Li cloud near the surface T_{vc} of about 3750 K, the average speed of the Li particles can be estimated with

$$v_{Li} = (2k_B T_{vc}/m_{Li})^{1/2}, \quad (8)$$

which is approximately 3×10^5 cm s^{-1}. Based on this velocity and the upper and lower Li surface density limits provided in Table 1, we can

determine the average Li mass flux with

$$f_{Li} = n_{Li} \cdot v_{Li} \cdot m_{Li}, \quad (9)$$

which yields approximately 1.7×10^{-19} – 5.3×10^{-19} g cm^{-2} s^{-1}.

Previous research indicates that high-speed meteoroid impacts, with velocities between 100 and 120 km/s, are considered the primary contributors to Mercury's surface impact vaporization rate[41]. Additionally, studies on meteoroid impactors on regolith targets have determined that the target-to-impactor mass ratios, Y, in impact-produced vapor clouds are approximately 100 for impacts at 90 km/s and approximately 180 for impacts at 120 km/s[42]. Therefore, it can be inferred that the mass ratio between the target and the impactor in the impact-produced vapor clouds on Mercury is approximately 150, assuming an average meteoroid impact velocity of 110 km/s.

The relative abundances of moderately volatile elements in meteorites can be compared. According to previous findings, Li and Na vary in carbonaceous chondrites only by about 30–40%[43,44]. This indicates that the composition of the meteorites might have been very similar. Indeed almost 85% of meteorite-falls on Earth are related to ordinary chondrites of types H (High total iron contents), L (Low total iron contents), and LL (Low total iron and low metal contents), with H and L types comprising about 70% of all impacts. Carbonaceous and enstatite chondrites together add about 6%, while achondrites and iron meteorites add about 5% and 2% of all falls, respectively. However, beside EL (Enstatit-chondrite with Low metal contents) chondrites, all chondrite types show similar Li/Na values between about $2.6 – 3.8 \times 10^{-4}$[44]. The Li/Na ratio, measured from meteoroid ablation in Earth's mesopause, is about 3.3×10^{-4}[9], which is consistent with this range.

The average atomic percentage of Na in ordinary chondrites is approximately 0.68%, whereas the total Na content in Mercury's exosphere is around 2.1%[45]. This suggests that the Na concentration on Mercury is about 3–4.3 times higher than that of chondrites. Taking into account that Mercury's surface composition is likely similar to that of enstatite or metal-rich chondrite meteorites[46], it can be inferred that Na has accumulated on the planet's uppermost layer over billions of years due to (micro-)meteoroid impacts. Since all alkali metals have a similar behavior, also Li is expected to enrich on Mercury. Assuming that the enrichment of Li on Mercury is comparable to that of the Na enrichment, the Li content on Mercury, χ_{pl}^{Li}, can be estimated from the average values of ordinary chondrites and is approximately $3 \times 10^{-4} \cdot 2.1$ Li at%, which corresponds to approximately 0.0006 at% or about 6 ppm[41]. Based on these values, the minimum and maximum total meteoroid mass flux, f_{tot},

$$f_{tot} = f_{Li}/(Y \times \chi_{pl}^{Li}), \quad (10)$$

during the detected events can be estimated and ranges between 1.9 and 5.9×10^{-16} g cm^{-2} s^{-1}. Considering that the Li content of the impacting meteorites χ_{imp}^{Li} is approximately 1.86 ppm[41], it's likely that the Li found in Mercury's exosphere primarily originates from the planet's surface.

Based on the minimum and maximum vertical column density, N, which ranges between 5.8×10^6 and 1.8×10^7 cm^{-2} (see Table 1), it is possible to give a rough estimate of the masses and sizes of the impacting meteoroids. Assuming that the Li column density is the same over the bombarded hemisphere of Mercury (i.e., the area of half of the planet: 3.74×10^{17} cm^2), the minimal and maximal number of Li atoms in the exosphere ranges between 2.2 and 6.7×10^{24}. By multiplying the minimal and maximal number of Li atoms by the atomic mass of Li (6.941 g/mol) and dividing by Avogadro's number 6.022×10^{23} mol^{-1}, the resulting minimal and maximal masses of the impact-produced Li in the exosphere are approximately 25 g and 77 g, respectively. Based on these impact-produced Li masses and

considering that the Li content in Mercury's exosphere is approximately 6 ppm, the total mass of the impact-produced vapor clouds is estimated to range between approximately 4.2×10^6 g and 1.8×10^7 g. Now, given that the target-to-impactor mass ratio, Y, in the impact-produced clouds is approximately 150, the mass of the impacting meteoroids, m_{imp}, is then expected to range between about 2.8×10^4 g and 1.2×10^5 g. Provided that the average mass density of the impacting meteoroids, ρ_{imp}, is approximately 3 g cm^{-3}, the minimal and maximal radii, r, of the impacting meteoroids,

$$r = (3 \cdot m_{imp}/(4 \cdot \pi \cdot \rho_{imp}))^{1/3}, \qquad (11)$$

range between approximately 13 cm and 21 cm, respectively. These values align closely with previous studies, which reported on impactors of similar size causing three short-term Na and Mg content enhancements in Mercury's exosphere[47].

In accordance with studies on the chemistry of the impact-produced vapor clouds, Li is expected to be delivered to the exosphere mainly during meteoroid impacts[39] with temperatures close to 3000–5000 K, whereas Li originating from the photolysis of impact-produced LiO and LiOH molecules are typically much hotter[48] but with smaller fractions. In addition to infalling (micro-)meteoritic and larger meteoritic material, lithophile elements such as Na, K, and Li can also be present in Mercury's regolith[15], where they can be released into the exosphere via photo-stimulated desorption, sputtering or thermal diffusion. Mercury's exosphere has a total Na column density of about 1.5×10^{11} cm^{-25}, which yields an average Li/Na ratio of about 5×10^{-5} during the studied impact events. Such values are smaller than the purely chondritic values mentioned above, suggesting that there must be significantly more Na in the exosphere than was delivered by the studied meteor events. This indicates that a significant fraction of Na in the exosphere comes from the regolith and not just from the event-related meteoritic material because Na is detected all the time, whereas Li is not.

The findings support the hypothesis that (micro-)meteoroids and larger meteoroids, which have continuously and sporadically impacted the surface of Mercury for billions of years, serve as a significant external source of volatile elements such as Na, K, and Li. This suggests that Mercury's surface has been modified and overlain by impact material, contributing substantially to Mercury's unexpectedly volatile-rich surface.

We expect that future measurements by the ESA/JAXA BepiColombo mission, in particular by the SERENA package[49,50] on board the Mercury Planetary Orbiter spacecraft[51], will help characterize the contribution of (micro-)meteoroid evaporation to the origin of Li and several other (yet-to-be-detected) heavy elements in the exosphere of Mercury. The discovery of Li at Mercury demonstrates the power of plasma physics methods in diagnosing the exospheric composition of planets using only magnetic field measurements. Hence, this method stands as a valuable complement to in-situ particle measurements, particularly when their availability is limited.

Methods

Pick-up ion cyclotron wave identification
In order to identify ICWs specifically produced by the pick up of freshly ionized lithium, we employ the same identification approach that was recently published for pick-up proton cyclotron waves[20,27]. Magnetic field observations at 20 Hz, collected by the MESSENGER spacecraft[2,52] between March 2011 and April 2015, are analyzed using a sliding interval of approximately 200 s, with the following procedures applied:

1. During each time interval, the magnetic field data are converted into a mean-field-aligned (MFA) coordinate system. The parallel component, $\hat{\mathbf{b}}_{\parallel} = \mathbf{B}_0/|\mathbf{B}_0|$, is derived from the average magnetic field over the interval, $\mathbf{B}_0 = [B_{x,0}, B_{y,0}, B_{z,0}]$. The

perpendicular components are computed as $\hat{\mathbf{b}}_{\perp 2} = \hat{\mathbf{b}}_{\parallel} \times [0, 0, 1]$ and $\hat{\mathbf{b}}_{\perp 1} = \hat{\mathbf{b}}_{\perp 2} \times \hat{\mathbf{b}}_{\parallel}$.

2. Each time interval of approximately 200 s (4096 data points) is divided into three sub-intervals of approximately 100 s (2048 data points), with a 50% overlap. For each sub-interval, the power spectral density matrix is computed[53]. Within the power spectral density matrix, the diagonal elements represent the in-phase power density of the parallel component ($P_{\parallel}$) and the perpendicular component ($P_{\perp} = \frac{1}{2} \cdot (P_{\perp 1} + P_{\perp 2})$). The off-diagonal elements correspond to the out-of-phase cross powers, where the complex part provides information on the ellipticity and handedness of the wave[54–57].

3. For the frequency range of interest, i.e., around the ion cyclotron frequency, the degree of polarization (DOP) is computed for each sub-interval to assess the coherence of the wave. A value of 100% signifies a pure state wave, while values below 70% indicate noise[57].

The arithmetic averages of the calculated power densities and ellipticities from the three sub-intervals are subsequently computed. A key criterion for ion cyclotron waves generated by local ion pick-up is that the observed wave frequency in both the spacecraft frame and plasma frame remains consistent and closely aligns with the local ion gyrofrequency[19]. To ensure reliable identification, the lithium gyro-frequency $f_{c,Li^+} = qB_0/(2\pi m_{Li})$ and its associated error range $\Delta f_{c,Li^+} = q\sigma_B/(2\pi m_{Li})$ are calculated for each approximately 200 s time interval. Here, ^{7}Li mass m_{Li}, charge q, along with the average and standard deviation of the magnetic field magnitude, B_0 and σ_B, are utilized. Subsequently, the same selection criteria that have been successfully applied in previous studies for the identification of pick-up ICWs around Venus and Mercury are employed[19,20]:

- The power density of each component is integrated over the frequency range $\Delta F = [0.8 \cdot (f_{c,Li^+} - \Delta f_{c,Li^+}), f_{c,Li^+} + \Delta f_{c,Li^+}]$ to account for power maxima occurring slightly below the computed gyrofrequency. Subsequently, the ratio of the (numerical) integrated perpendicular fluctuations ($E_{\perp} = \int_{\Delta F} P_{\perp} df$) to parallel fluctuations ($E_{\parallel} = \int_{\Delta F} P_{\parallel} df$) is calculated, which must satisfy the condition $E_{\perp}/E_{\parallel} > 5$ to ensure that the observed waves are transverse.

- Within the frequency range ΔF, the ellipticity must satisfy the condition $\epsilon < -0.5$ to confirm left-handed polarization of the observed wave in the spacecraft frame.

- To ensure substantial coherence of the observed wave and a high signal-to-noise ratio, the degree of polarization (DOP) for each sub-interval within ΔF must exceed 0.7.

- The maximum of the perpendicular fluctuating field ($P_{\perp}$) lies within ΔF, ensuring that the observed wave's dominant mode corresponds to the ion cyclotron mode.

- Only time intervals during which MESSENGER was situated within the solar wind[58,59], and at least 10 min away from the bow shock, are preselected to ensure that solely upstream waves are considered[19].

These five selection criteria ensure that only upstream waves exhibiting the defining characteristics of pick-up ion cyclotron waves are included. Over four (Earth) years of MESSENGER observations, 28 time intervals meet the selection criteria.

Estimation of injection velocity
Given the limitations of MESSENGER's plasma measurements, a solar wind propagation model[60] provided by the AMDA database[61] is employed. This model, which has been successfully applied to Mercury[20,27], offers approximate estimates of the solar wind's plasma density (n_{SW}) and velocity (V_{SW}) during the ICW observation period. The injection velocity ($\mathbf{V}_{inj}$) is defined as the aberrated solar wind

Table 2 | Observation time of the 28 time intervals that fulfill the ICW selection criteria

Year	Month	Day	Time (UTC)	SZA	Study event
2011	04	02	19:29	71°	
2011	04	02	19:41	70°	*
2011	04	03	07:41	72°	*
2011	04	03	08:56	62°	*
2011	04	03	11:45	42°	*
2011	12	26	18:09	80°	
2011	12	26	18:15	79°	*
2011	12	26	18:21	79°	
2012	02	07	12:22	108°	
2012	03	05	16:26	69°	*
2012	05	27	19:04	85°	*
2012	11	30	15:08	31°	*
2012	12	01	04:09	94°	
2012	12	01	13:11	90°	
2012	12	01	20:52	71°	*
2012	12	01	20:59	70°	
2013	05	01	01:59	46°	*
2013	05	01	02:03	49°	
2013	05	01	02:07	50°	
2013	05	01	02:10	50°	
2013	11	15	19:48	114°	
2013	12	05	05:00	109°	
2013	12	18	22:52	95°	
2014	01	13	13:01	73°	
2014	01	13	13:16	71°	*
2014	07	24	07:16	66°	*
2014	10	03	15:22	93°	
2015	04	12	18:03	92°	

The solar zenith angle (SZA) is defined as angle between the aberrated solar wind velocity vector and the S/C observation location. The 12 independent ICW events used in this study are marked with an asterisk.

Fig. 4 | **Position of the observed Li⁺ ICW events. a** Observation location in Mercury Solar Orbital (MSO) and **b** Mercury electromagnetic (MBE) coordinates. In this coordinate system, $+X_{MBE}$ aligns with the Sun along the Li⁺ ion injection velocity, V_{inj}, $+Y_{MBE}$ aligns with the background magnetic field $\mathbf{B}_O$, and $+Z_{MBE}$ aligns with the convection electric field $\mathbf{E} = \mathbf{V}_{inj} \times \mathbf{B}_O$. The color-scale in panel **b** indicates the velocity ratio between the Alfvén speed, V_A, and the injection velocity, V_{inj}. Source data are provided as a Source Data file.

velocity ($\mathbf{V}_{SW}$), adjusted by Mercury's orbital motion ($\mathbf{V}_{Mercury}$). Mercury's orbital motion is determined using the Navigation and Ancillary Information Facility[62,NAIF] through the WebGeocalc toolkit, employing ECLIPJ2000 coordinates with Mercury set as the target, the Sun as the observer, and the event observation time as the input. Consequently, the injection velocity is expressed as $\mathbf{V}_{inj} = -\mathbf{V}_{SW} + \mathbf{V}_{Mercury}$.

The injection velocity vector is additionally utilized to calculate the solar zenith angle (SZA). The SZA is subsequently employed to identify events occurring on the dayside of the terminator (SZA < 90°), ensuring that the observed waves are freshly generated through local ion pick-up[26,27]. Of the 28 preselected time intervals, 20 correspond to observations made on the dayside of the terminator (see Table 2).

Due to the limiting factor of the selection window size (approximately 200 s) the number of events is overestimated, since unique ICW events may continue up to approximately 900 s. From the 20 time intervals, 12 events are identified as independent ICW events.

Figure 4a shows the observation location of the 12 events in Mercury–Solar–Orbital (MSO) coordinates, $+X_{MSO}$ points toward the sun, $+Y_{MSO}$ lies in the orbital plane, perpendicular to X_{MSO} and opposite to the direction of planetary orbital motion, and $+Z_{MSO}$ is normal to the orbital plane and positive northward. To verify that the identified ICWs are locally generated through the initial ionization of neutral lithium (Li), the observation locations are transformed into an local electromagnetic (MBE) coordinate system to investigate potential asymmetries relative to the convection electric field. Figure 4b illustrates the positions of the 12 ICWs within the local MBE coordinate
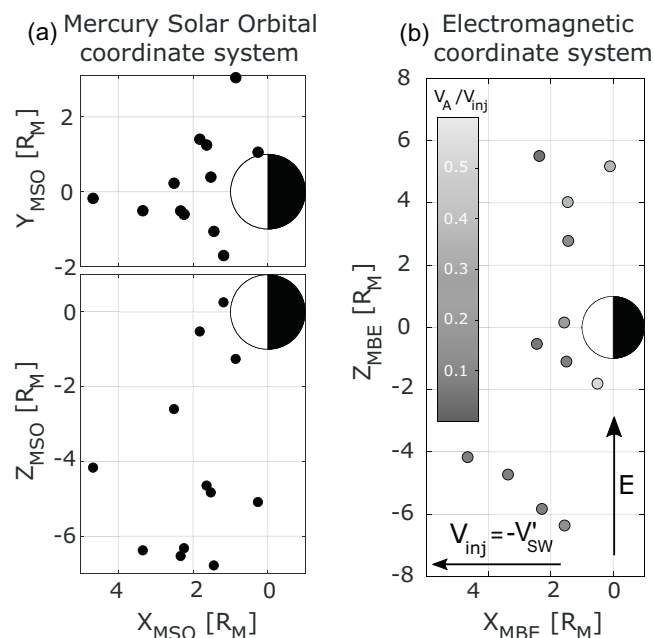
system. In this system, the X_{MBE} axis is oriented positively towards the Sun and directed opposite to the aberrated solar wind velocity vector ($\mathbf{V}'_{SW}$), which corresponds to the injection velocity of Li⁺ ions into the solar wind plasma ($\mathbf{V}_{inj} = -\mathbf{V}'_{SW}$). The Y_{MBE} axis is aligned positively with the background magnetic field component ($\mathbf{B}_O$), while the Z_{MBE} axis is oriented positively in the direction of the convection electric field ($\mathbf{E} = \mathbf{V}_{inj} \times \mathbf{B}_O$).

Figure 4b provides several indications that the observed ICWs are generated locally: (1) The majority of ICWs are detected at large positive X_{MBE}, far from the planet, implying that they would have had to propagate against the solar wind flow at velocities exceeding the solar wind speed. This scenario is incompatible with the observations, as ICWs generally propagate at speeds comparable to or lower than the local Alfvén velocity (V_A), and the Alfvén velocity associated with the detected ICWs is significantly smaller than the aberrated solar wind speed, which defines the injection velocity of the ions into the solar wind ($V_A/V_{inj} < 0.6$). (2) ICWs are distributed symmetrically across the $\pm Z_{MBE}$ hemispheres. Since there is no known mechanism capable of transporting ions across the magnetic field against the electric field into the region of negative motional electric field, the ICWs must have been generated locally[19]. Based on this analysis, we conclude that the 12 ICWs are indeed locally generated, validating the underlying assumptions required for reliable on-site density estimation.

Photoionization rate

The photoionization rate significantly varies with the solar activity and the heliocentric distance of Mercury to the Sun. Since the photoionization rate is important to obtain a reliable Li density estimation, we modify the ionization rate, $k_{h\nu}$, in Eq. (5) as follows: As the first step to provide an estimate of solar activity, the FISM-P irradiance, derived from the Flare Irradiance Spectral Model[63], FISM-P for Mercury, is normalized to the range [0, 1]. Here, 0 corresponds to 0.028 Wm⁻²s⁻¹nm⁻¹ and 1 corresponds to 0.1 Wm⁻²s⁻¹nm⁻¹, representing the minimum and maximum spectral irradiance indices at 121.5 nm during solar cycle 24. In the

second step, the normalized FISM-P irradiance index is used to interpolate the corresponding photoionization rate at Earth's orbit, ranging between a minimum of $1.97 \times 10^{-4}\,s^{-1}$ (quiet Sun = 0) and a maximum of $2.07 \times 10^{-4}\,s^{-1}$ (active Sun = 1)[64]. In the final step, this ionization rate is rescaled from Earth's orbit (1 AU) to Mercury's heliocentric distance during the ICW observation period, which varies between 0.31 AU and 0.47 AU, by applying the inverse square law.

Monte Carlo error analysis

To capture the effect of uncertainty of the parameters (V_A, V_{inj}, α, Φ, and the characteristic time $\Omega_{c,Li^+} \cdot t$) used in Eqs. (2) and (5) on the derived Li densities, we applied a Monte Carlo error propagation with 50,000 samples.

We use the error information about the solar wind propagation model[60] and assume that the solar wind velocity and density, obtained from the solar wind propagation model, are normal-distributed about the values predicted by the model with a variance of 50 km/s in each velocity component and a variance of $5\,cm^{-3}$ for the solar wind density. In addition we varied the efficiency parameter Φ according to a beta-distribution, $\mathcal{Be}(\Phi; 3, 6)$, that has an expectation value of $\langle \Phi \rangle = 0.3$, as shown by simulations[29]. We also normally distributed the characteristic time for the ICW development ($\Omega_{c,Li^+} \cdot t$) around 100 gyroperiods with a variance of 40 gyroperiods (conservative estimate), as found in simulations[29].

Data availability

All data analyzed in this work are publicly available: The magnetic field (MAG) data (Version ID: 1.0) from the MESSENGER spacecraft is public available at the NASA Planetary Data System (PDS) and can be retrieved on their website[65]: https://pds-ppi.igpp.ucla.edu/collection/urn:nasa:pds:mess-mag-calibrated:data-mso. The solar wind density and velocity data were obtained from the Automated Multi-Dataset Analysis (AMDA)[61] database. All data are open-access and can be downloaded on their website via the Workspace Explorer under: Solar Wind Propagation Models/Mercury/Tao Model/SW/Input OMNI: http://amda.cdpp.eu/. The orbital motion of Mercury was retrieved from the Navigation and Ancillary Information Facility (NAIF)[62], publicly accessible on the NASA Jet Propulsion Laboratory (JPL) webpage: https://wgc.jpl.nasa.gov:8443/webgeocalc/#StateVector The solar spectral irradiance at the orbit of Mercury that was used to determine the solar activity during the event observations was obtained from the Flare Irradiance Spectral Model for Mercruy (FISM-P), provided by the LASP Interactive Solar iRradiance Datacenter[63], publicly accessible on their webpage: https://lasp.colorado.edu/lisird/data/fism_p_ssi_mercury/. Source data are provided with this paper and the datasets analyzed during the current study are available from the corresponding author upon request. Source data are provided with this paper.

References

1. Broadfoot, A. L., Kumar, S., Belton, M. J. S. & McElroy, M. B. Mercury's atmosphere from Mariner 10: preliminary results. *Science* **185**, 166–169 (1974).
2. Solomon, S. C., McNutt Jr, R. L., Gold, R. E. & Domingue, D. L. MESSENGER mission overview. *Space Sci. Rev.* **131**, 3 – 39 (2007).
3. McClintock, W. E. et al. Observations of Mercury's exosphere: composition and structure. In: (eds Solomon, C., Nittler, L. R. & Anderson, B. J.) *Mercury: the View After MESSENGER*, pp 407–429 (Cambridge University Press, Cambridge, UK, 2018).
4. Fjeldbo, G. et al. The occultation of Mariner 10 by Mercury. *Icarus* **29**, 439–444 (1976).
5. Killen, R. et al. Processes that promote and deplete the exosphere of Mercury. *Space Sci. Rev.* **132**, 433–509 (2007).
6. Potter, A. & Morgan, T. Discovery of sodium in the atmosphere of Mercury. *Science* **229**, 651–653 (1985).
7. Potter, A. E. & Morgan, T. H. Potassium in the atmosphere of Mercury. *Icarus* **67**, 336–340 (1986).
8. Morgan, T. H., Zook, H. A. & Potter, A. E. Impact-driven supply of sodium and potassium to the atmosphere of Mercury. *Icarus* **75**, 156–170 (1988).
9. Plane, J. M. C. The chemistry of meteoric metals in the Earth's upper atmosphere. *Int. Rev. Phys. Chem.* **10**, 55–106 (1991).
10. Marchi, S., Morbidelli, A. & Cremonese, G. Flux of meteoroid impacts on Mercury. *Astron. Astrophys.* **431**, 1123–1127 (2005).
11. Jasinski, J. M. et al. A transient enhancement of Mercury's exosphere at extremely high altitudes inferred frompickup ions. *Nat. Commun.* **11**, 4350 (2020).
12. Korotev, R. L. The nature of the meteoritic components of Apollo 16 soil, as inferred from correlations of iron, cobalt, iridium, and gold with nickel. *J. Geophys. Res.* **92**, E447–E461 (1987).
13. Korotev, R. L. Some things we can infer about the Moon from the composition of the Apollo 16 regolith. *Meteoritics* **32**, 447–478 (1997).
14. Janches, D. et al. Meteoroids as one of the sources for exosphere formation on airless bodies in the inner Solar system. *Space Sci. Rev.* **217**, 50 (2021).
15. Sprague, A. L., Hunten, D. M. & Grosse, F. A. Upper limit for lithium in Mercury's atmosphere. *Icarus* **11**, 345–349 (1996).
16. Doressoundiram, A., Leblanc, F., Foellmi, C. & Erard, S. Metallic species in Mercury's exosphere: EMMI/New technology telescope observations. *Astrophys. J.* **137**, 3859–3863 (2009).
17. Huddleston, D. E. & Johnstone, A. D. Relationship between wave energy and free energy from pickup ions in the comet Halley environment. *J. Geophys. Res.* **97**, 12217–12230 (1992).
18. Mazelle, C. et al. Bow shock and upstream phenomena at Mars. *Space Sci. Rev.* **111**, 115 – 118 (2004).
19. Delva, M., Zhang, T. L., Volwerk, M., Vörös, Z. & Pope, S. A. Proton cyclotron waves in the solar wind at Venus. *Geophys. Res. Lett.* **113**, E00B06 (2008).
20. Schmid, D. et al. Pick-up ion cyclotron waves around Mercury. *Geophys. Res. Lett.* **48**, e2021GL092606 (2021).
21. James, M. K. et al. Interplanetary magnetic field properties and variability near Mercury's orbit. *J. Geophys. Res.* **122**, 7907–7924 (2017).
22. Delva, M. et al. Proton cyclotron wave generation mechanisms upstream of Venus. *J. Geophys. Res.* **116**, A02318 (2011).
23. Chamberlain, J. W. Planetary coronae and atmospheric evaporation. *Planet. Space Sci.* **11**, 901–960 (1963).
24. Gary, S. P. Electromagnetic ion/ion instabilities and their consequences in space plasmas: a review. *Space Sci. Rev.* **56**, 373–415 (1991).
25. Michiels, E. & De Bièvre, P. Absolute isotopic composition and the atomic weight of a natural sample of lithium. *Int. J. Mass Spectrom. Ion. Phys.* **49**, 265–274 (1983).
26. Delva, M. et al. Hydrogen in the extended Venus exosphere. *Geophys. Res. Lett.* **36**, L01203 (2009).
27. Schmid, D. et al. Magnetic evidence for an extended hydrogen exosphere at Mercury. *J. Geophys. Res.* **127**, e2022JE007462 (2022).
28. Cowee, M. M., Winske, D., Russell, C. T. & Strangeway, R. J. 1D hybrid simulations of planetary ion-pickup: energy partition. *Geophys. Res. Lett.* **34**, L02113 (2007).
29. Cowee, M. M., Gary, S. P. & Wei, H. Y. Pickup ions and ion cyclotron wave amplitudes upstream of Mars: first results from the 1D hybrid simulation. *Geophys. Res. Lett.* **39**, L08104 (2012).
30. Wurz, P. et al. Particles and photons as drivers for particle release from the surfaces of the Moon and Mercury. *Space Sci. Rev.* **218**, 10 (2022).
31. Killen, R., Benkhoff, J. & Morgan, T. Mercury's polar caps and the generation of an OH exosphere. *Icarus* **125**, 195–211 (1997).
32. Killen, R. M. & Ip, W.-H. The surface-bounded atmospheres of Mercury and the Moon. *Rev. Geophys.* **37**, 361–406 (1999).

33. Sun, W. et al. MESSENGER observations of planetary ion enhancements at Mercury's northern magnetospheric cusp during flux transfer event showers. *J. Geophys. Res.* **127**, e2022JA030280 (2022).

34. Slavin, J. A. et al. MESSENGER observations of Mercury's dayside magnetosphere under extreme solar wind conditions. *J. Geophys. Res.* **119**, 8087–8116 (2014).

35. Mangano, V. et al. Dynamical evolution of sodium anisotropies in the exosphere of mercury. *Planet. Space Sci.* **82-83**, 1–10 (2013).

36. Winslow, R. M. et al. Interplanetary coronal mass ejections from MESSENGER orbital observations at Mercury. *J. Geophys. Res.* **120**, 6101–6118 (2015).

37. Mura, A. Loss rates and time scales for sodium at mercury. *Planet. Space Sci.* **63-64**, 2–7 (2012).

38. Mangano, V. et al. The contribution of impulsive meteoritic impact vapourization to the hermean exosphere. *Panet. Space Sci.* **55**, 1541–1556 (2007).

39. Berezhnoy, A. A., Belov, G. V. & Wöhler, C. Chemical processes during collisions of meteoroids with the Moon. *Planet. Space Sci.* **249**, 105942 (2024).

40. Eichhorn, G. Heating and vaporization during hypervelocity particle impact. *Planet. Space Sci.* **26**, 463–467 (1978).

41. Pokorný, P., Sarantos, M. & Janches, D. A comprehensive model of the meteoroid environment around Mercury. *Astrophys. J.* **863**, 31 (2018).

42. Cintala, M. J. Impact-induced thermal effects in the lunar and mercurian regoliths. *J. Geophys. Res.* **97**, 947–973 (1992).

43. Palme, H., Larimer, J. W. & Lipschutz, M. E. Moderately volatile elements. In: *Meteorites and the Early Solar System*, vol. A89-27476, pp 10–91 (1988).

44. Wasson, J. T. & Kallemeyn, G. W. Compositions of chondrites. *Philos. Trans. Roy. Soc. Lond.* **325**, 535–544 (1988).

45. Peplowski, P. N. et al. Enhanced sodium abundance in Mercury's north polar region revealed by the MESSENGER Gamma-Ray Spectrometer. *Icarus* **228**, 86–95 (2014).

46. Nittler, L. R., Chabot, N. L., Grove, T. L. & Peplowski, P. N. The chemical composition of Mercury. *Cambridge Planetary Science*, pp 30–51 (Cambridge University Press, 2018).

47. Cassidy, T. A., Schmidt, C. A., Merkel, A. W., Jasinski, J. M. & Burger, M. H. Detection of large exospheric enhancements at Mercury due to meteoroid impacts. *Planet. Sci. J.* **2**, 175 (2021).

48. Valiev, R. R. et al. Photolysis of diatomic molecules as a source of atoms in planetary exospheres. *Astron. Astophys.* **633**, A39 (2020).

49. Orsini, S. et al. SERENA: particle instrument suite for determining the Sun-Mercury interaction from BepiColombo. *Space Sci. Rev.* **217**, 11 (2021).

50. Orsini, S. et al. Correction to: SERENA: particle instrument suite for determining the Sun-Mercury interaction from BepiColombo. *Space Sci. Rev.* **217**, 30 (2021).

51. Benkhoff, J. et al. BepiColombo—mission overview and science goals. *Space Sci. Rev.* **217**, 90 (2021).

52. Anderson, B. J. et al. The magnetometer instrument on MESSENGER. *Space Sci. Rev.* **131**, 417 – 450 (2007).

53. Welch, P. The use of fast Fourier transform for the estimation of power spectra: a method based on time averaging over short, modified periodograms. *IEEE Trans. Audio Electroacoust.* **15**, 70–73 (1967).

54. Means, J. D. Use of the three-dimensional covariance matrix in analyzing the polarization properties of plane waves. *J. Geophys. Res.* **77**, 5551–5559 (1972).

55. Fowler, R. A., Kotick, B. J. & Elliott, R. D. Polarization analysis of natural and artificially induced geomagnetic micropulsations. *J. Geophys. Res.* **72**, 2871–2883 (1967).

56. Arthur, C., McPherron, R. L. & Means, J. D. A comparitive study of three techniques for using the spectral matrix in wave analysis. *Radio Sci.* **11**, 833–845 (1976).

57. Samson, J. C. & Olson, J. V. Some comments on the descriptions of the polarization states of waves. *Geophys. J. Int.* **61**, 115–129 (1980).

58. Winslow, R. M. et al. Mercury's magnetopause and bow shock from MESSENGER magnetometer observations. *J. Geophys. Res.* **118**, 2213–2227 (2013).

59. Philpott, L. C., Johnson, C. L., Anderson, B. J. & Winslow, R. M. The shape of Mercury's magnetopause: the picture from MESSENGER magnetometer observations and future prospects for BepiColombo. *J. Geophys. Res.* **125**, e2019JA027544 (2020).

60. Tao, C., Kataoko, R., Fukunishi, H., Takahashi, Y. & Yokokama, T. Magnetic field variations in the Jovian magnetotail induced by solar wind dynamic pressure enhancements. *J. Geophys. Res.* **110**, A11208 (2005).

61. Génot, V. et al. Automated Multi-Dataset Analysis (AMDA): an on-line database and analysis tool for heliospheric and planetary plasma data. *Planet. Space Sci.* **201**, 105214 (2021).

62. Acton, H. C. Ancillary data services of NASA's Navigation and Ancillary Information Facility. *Planet. Space Sci.* **44**, 65–70 (1996).

63. Chamberlin, P. C., Woods, T. N. & Eparvier, F. G. Flare Irradiance Spectral Model (FISM): flare component algorithms and results. *Space Weather* **6**, S05001 (2008).

64. Huebner, W. & Mukherjee, J. Photoionization and photodissociation rates in solar and blackbody radiation fields. *Planet. Space Sci.* **106**, 11–45 (2015).

65. Korth, H. MESSENGER MAG Calibrated MSO Coordinates Science Data Collection. *NASA Planetary Data System* (2021).

Acknowledgements

Author contributions

D.S. initiated the study, performed the analysis, and led the writing of the paper. H.L. provided the foundational concept of the exospheric model to interpret the observational results and contributed to both writing and editing the paper. A.A.B. contributed in discussion of the results and writing. F.B. and M.S. analyzed the origin of Li and assisted in the evaluation of the paper. F.P. and M.V. contributed to the development of the analysis method and supported the editing of the paper. A.V., C.S.W., W.B., R.N., and G.M. provided assistance with manuscript editing and participated in the evaluation of the study's results and discussion.

Competing interests

The authors declare no competing interests.

Additional information

Supplementary information The online version contains supplementary material available at https://doi.org/10.1038/s41467-025-61516-4.

Correspondence and requests for materials should be addressed to Daniel Schmid.

Peer review information *Nature Communications* thanks David Schriver, and the other, anonymous, reviewers for their contribution to the peer review of this work. A peer review file is available.

Reprints and permissions information is available at http://www.nature.com/reprints

Publisher's note Springer Nature remains neutral with regard to jurisdictional claims in published maps and institutional affiliations.